Performance of a Vibration Isolator with Sigmoidal Force-Deflection Curve

https://doi.org/10.1177/1077546322113900 6

G. Gatti[a*] and C. Svelto[b]

[a] *Dipartimento di Ingegneria Meccanica, Energetica e Gestionale, Università della Calabria, Rende, Italy*

[b] *Dipartimento di Elettronica, Informazione e Bioingegneria, Politecnico di Milano, Milan, Italy*

* Corresponding author:

G. Gatti, Department of Mechanical, Energy and Management Engineering, University of Calabria, Via P. Bucci 46C, 87036 Rende (CS), Italy – email: gianluca.gatti@unical.it

ABSTRACT

This paper presents a theoretical insight on the performance of a vibration isolator consisting of a combination of linear mechanical springs arranged to achieve a specific form of geometric nonlinearity. In particular, positive and negative stiffness nonlinearities are combined to achieve a sigmoidal shape of the force-deflection curve, which is proven to be beneficial for vibration isolation purposes when the amplitude of vibration is relatively large. Such behaviour is fundamentally different from that of the classical quasi-zero-stiffness isolator, which presents a low dynamic stiffness at the equilibrium configuration and is thus effective for relatively low amplitude of vibration. The analytical findings are validated by numerical simulations, providing useful guidelines for the design of such isolators.

1 INTRODUCTION

The introduction of nonlinear elements to improve the dynamic performance of vibration isolators has been largely pursued in the last decades (Ibrahim, 2008), and both nonlinear stiffness and nonlinear damping have been investigated (Mofidian and Bardaweel, 2018). The main advantage achieved using a nonlinear elastic element is the possibility to achieve a high-static-low-dynamic behaviour, and cope with the simultaneous competing requirements of improving the isolation region (which would require a relatively soft stiffness) and statically supporting the load (which would require a relatively hard stiffness) (Yang et al., 2021). This results in the so-called quasi-zero-stiffness (QZS) isolator, which has been extensively investigated in its essential three-spring configuration, both in theory (Kovacic et al., 2008) and experiments (Xu et al. 2014). The theoretical fundamental performance of an ideal zero-stiffness suspension has also been studied for shock isolation (Liu et al., 2014). The QZS behaviour is generally obtained by combining positive and negative (e.g. bi-stable) elastic elements, where the former may be conveniently achieved by linear springs aligned with the direction of motion, and the latter may be formed in a variety of

ways, for example by combination of flexible beams and linkages (Zhu et al., 2022), buckling beams or plates (Zhang et al., 2022b; Liu et al., 2013), inclined coil spring arrangements (Zhang et al. 2022a; Gatti, 2021b), combination of springs and linkages (Dai et al., 2018; Shaw et al., 2021, Gatti et al., 2022; Gatti, 2022; Jing et al., 2022), cam mechanisms (Li et al., 2020; Zou et al., 2021) and several bio-inspired structures (Song et al., 2022; Shi et al., 2022; Yan et al., 2021), including configurations inspired by skeletal muscles (Gatti, 2021a; Gatti, 2019). A nonlinear-stiffness and nonlinear-inertial vibration isolator has been proposed in (Wang et al., 2021), where the nonlinear inertial characteristic is implemented via a geometrical nonlinear inerter producing nonlinear acceleration. Regarding nonlinear damping, for example, it has been investigated with reference to a rubber-based vehicle seat suspension in (Zhao et al., 2018), and also introduced on purpose to outperform the linear system in some cases (Tang and Brennan, 2013). Identification of nonlinear stiffness and damping parameters has been proposed in (Lu et al., 2019) based on the jump phenomenon.

Recently, a preliminary investigation on the static and dynamic performance of a suspension system consisting of two pairs of inclined spring has been proposed in (Gatti, 2020), highlighting the possibility to achieve a symmetric sigmoidal force-deflection curve with low stiffness region far from the static equilibrium condition. Following that, several studies have exploited that main idea to develop improved vibration isolators. In particular, Zhao et al. (2021a) first proposed an isolator with two pairs of oblique springs to increase the QZS region around the static equilibrium configuration, and then investigated the use of three pairs of springs (Zhao et al., 2021b), discovering a nearly horizontal straight-line behaviour near the equilibrium position in the stiffness curve. On this trend, following the study presented in (Gatti, 2019), asymmetric force-deflection curve has also been adopted to realise large stroke quasi-zero stiffness vibration isolator using a three-link mechanism (Yan et al., 2020).

The main idea exploited in the application of vibration isolation has thus been to enlarge the QZS region around the static equilibrium configuration where the stiffness is theoretically zero. The

larger that region the better the isolation performance. An isolator exploiting such configuration is denoted hereafter as Single-Quasi-Zero-Stiffness (SQZS) isolator, and has just one QZS region around the static equilibrium configuration. It is characterised by having an elastic suspension with very low stiffness at small deflections, which then increases in a hardening way for larger deflections.

In this paper we present a complimentary study, where two pairs of oblique springs are used to achieve a tailored shape of the force-deflection curve, resulting in two symmetrical QZS regions away from the static equilibrium configuration. The corresponding isolator is denoted hereafter as Double-Quasi-Zero-Stiffness (DQZS) isolator, and it is characterised by having an elastic suspension where the stiffness is relatively large at the static equilibrium configuration and then decreases in a softening way for larger deflections.

The SQZS and DQZS configuration are thus compared to highlight the benefits and the useful range of parameters where the latter outperforms the former.

Following this introduction, the paper is organised as follows. Section 2 presents the model of the DQZS isolator and links its parameters to those of the SQZS isolator for a reasonable comparison. Section 3 enters the details of the elastic suspension from the static point of view, and Section 4 compares the dynamic performance of the two isolators. Section 5 draws the conclusions.

2 MODEL OF THE ISOLATOR

The proposed model of vibration isolator is inspired by skeletal muscles (Gatti, 2019) and is illustrated in Fig. 1(a), in both its unloaded (grey) and loaded (black) configuration, subject to the weight of the mass *m* to be isolated. It is assumed that gravity is acting downwards along the vertical direction. The suspension system consists of four linear springs attached to a rectangular support structure (the external frame), as detailed in Fig.1(a), so that when the mass moves the springs rotate and change their length accordingly. It is assumed that the suspension system is symmetric respect to the vertical axis, and when the static configuration is achieved due to the

weight of the mass m, symmetry is attained with respect to the horizontal axis as well. The motion of the isolated mass is assumed to be constrained to the vertical direction only, and its position is denoted by y_r, relative to the static equilibrium configuration. In the unloaded case, the mass position is $y_r = y_0$, as illustrated in the schematic of Fig. 1(a), and depends on the free length of the springs. The upper springs have linear stiffness k_{s1}, and the lower springs have linear stiffness k_{s2}. The geometry of the springs arrangement is defined by the dimensions a and d, as indicated in the schematic of Fig. 1(a). The system is supposed to be excited at its base by an imposed external harmonic displacement y_e.

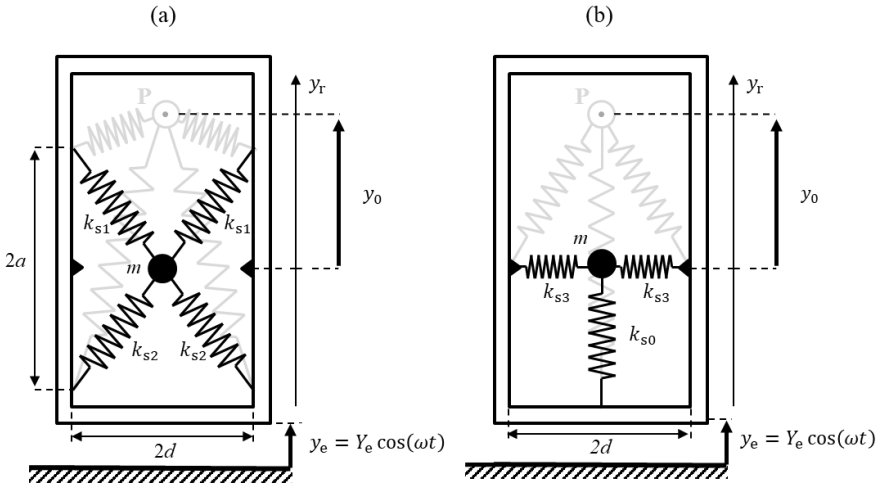

Fig. 1 Schematic of (a) the proposed DQZS isolator and (b) the classical SQZS isolator.

The proposed DQZS isolator of Fig. 1(a) is compared to the classical SQZS isolator (Kovacic et al., 2008), which is illustrated in the schematic of Fig. 1(b). In the case of the SQZS isolator, the isolated mass m is supported by a vertical linear spring with stiffness k_{s0}, and the low dynamic stiffness effect is achieved by a negative stiffness component obtained by a pair of lateral linear springs having stiffness k_{s3}, which attain a horizontal configuration under the weight of the suspended mass, as illustrated in the schematic of Fig.1(b).

The comparison between the two nonlinear isolators is performed on the assumption of the same isolated mass m, the same width $2d$ (which mainly defines the size of the device), and the same

static deflection y_0. A comparison to the linear case, having one vertical spring only, is also reported for completeness.

3 ISOLATOR SUSPENSION

To facilitate the comparisons among the different isolators, the classical nonlinear isolator with T-shape configuration and SQZS behaviour (Kovacic et al., 2008) is briefly reviewed below.

3.1 Classical isolator suspension with SQZS behaviour

The vertical static force-displacement characteristic at the suspension point P in the schematic of Fig. 1(b) is given by the sum of three components, as

$$f_{\mathrm{SQZS}} = k_{s0}(y_{\mathrm{r}} - y_0) + k_{\mathrm{s3}} y_r \left(1 - \frac{\sqrt{d^2 + {y_0}^2}}{\sqrt{d^2 + {y_{\mathrm{r}}}^2}}\right) + mg \tag{1}$$

where the first component is linear and corresponds to the force acting on the suspension point P due to the vertical spring, the second component is nonlinear due to the lateral springs, and the third component is the weight of the mass due to the acceleration of gravity, g.

Equation (1) can be normalized by d and k_{s0} to yield

$$\hat{f}_{\mathrm{SQZS}} = (\hat{y}_{\mathrm{r}} - \hat{y}_0) + \hat{k}_{\mathrm{s3}} \hat{y}_r \left(1 - \frac{\sqrt{1 + {\hat{y}_0}^2}}{\sqrt{1 + {\hat{y}_{\mathrm{r}}}^2}}\right) + \hat{p} \tag{2}$$

where $\hat{f}_{\mathrm{SQZS}} = \frac{f_{\mathrm{SQZS}}}{k_{\mathrm{s0}}} d, \hat{k}_{\mathrm{s3}} = \frac{k_{\mathrm{s3}}}{k_{\mathrm{s0}}}, \hat{y}_r = \frac{y_{\mathrm{r}}}{d}, \hat{y}_0 = \frac{y_0}{d}$ and $\hat{p} = \frac{mg}{k_{\mathrm{s0}} d}$ are now dimensionless variables.

Imposing both the static equilibrium configuration and the SQZS behaviour at $\hat{y}_{\mathrm{r}} = 0$, gives the following relations

$$\hat{p} = \hat{y}_0 \tag{3a}$$

$$\hat{k}_{s3} = \frac{1}{2\left(\sqrt{1+\hat{y}_0^2}-1\right)} \tag{3b}$$

so that Eq. (2) reduces to

$$\hat{f}_{SQZS} = \hat{y}_r \frac{\sqrt{1+\hat{y}_0{}^2}}{\sqrt{1+\hat{y}_0{}^2}-1}\left(1 - \frac{1}{\sqrt{1+\hat{y}_r{}^2}}\right) \tag{4}$$

Note that the initial stiffness of the force-deflection curve is zero, i.e. $\left.\frac{\partial \hat{f}_{SQZS}}{\partial \hat{y}_r}\right|_{\hat{y}_r=0} = 0$, and that Eq.(3a) imposes that the normalized weight is equal to the normalized static displacement.

The normalized force-deflection curve of the corresponding linear isolator is instead $\hat{f}_{LIN} = \hat{y}_r$.

3.2 Proposed isolator suspension with DQZS behaviour

The vertical static force-displacement characteristic at the suspension point P in the schematic of Fig. 1(a) is again given by the sum of three components, as

$$f_{DQZS} = 2k_{s1}(y_r - a)\left(1 - \frac{\sqrt{d^2+(a-y_0)^2}}{\sqrt{d^2+(a-y_r)^2}}\right) + 2k_{s2}(a + y_r)\left(1 - \frac{\sqrt{d^2+(a+y_0)^2}}{\sqrt{d^2+(a+y_r)^2}}\right) + mg \tag{5}$$

where the first nonlinear component is the force acting on the suspension point P due to the upper pair of springs, the second nonlinear component is due to the lower pair of springs, and the third constant component is the weight of the mass.

Equation (5) may be also normalized as

$$\hat{f}_{DQZS} = \hat{k}_{s1}(\hat{y}_r - \hat{a})\left(1 - \sqrt{\frac{1+(\hat{a}-\hat{y}_0)^2}{1+(\hat{a}-\hat{y}_r)^2}}\right) + \hat{k}_{s2}(\hat{a} + \hat{y}_r)\left(1 - \sqrt{\frac{1+(\hat{a}+\hat{y}_0)^2}{1+(\hat{a}+\hat{y}_r)^2}}\right) + \hat{p} \tag{6}$$

where $\hat{f}_{\mathrm{DQZS}} = \frac{f_{\mathrm{DQZS}}}{k_{\mathrm{s0}} d}$, $\hat{k}_{\mathrm{s1}} = \frac{k_{\mathrm{s1}}}{k_{\mathrm{s0}}}$, $\hat{k}_{\mathrm{s2}} = \frac{k_{\mathrm{s2}}}{k_{\mathrm{s0}}}$, $\hat{a} = \frac{a}{d}$ and $\hat{y}_0 = \frac{y_0}{d}$.

For dynamic purposes, as detailed further below, the static force-displacement curve is approximated by an odd function of the displacement (i.e. the suspension is acting the same way in tension and compression), exhibiting a DQZS behaviour.

To this end, firstly, the zero- and second-order Taylor series coefficients of Eq. (6) are set to zero, yielding the following relations among the system parameters

$$\hat{k}_{s1} = \frac{\hat{y}_0}{2\hat{a}\left(1-\frac{\hat{l}_{01}}{\hat{l}_{02}}\right)} \tag{7a}$$

$$\hat{k}_{s2} = \frac{\hat{y}_0}{2\hat{a}\left(\frac{\hat{l}_{02}}{\hat{l}_{01}}-1\right)} \tag{7b}$$

where $\hat{l}_{01} = \sqrt{1+(\hat{a}-\hat{y}_0)^2}$ and $\hat{l}_{02} = \sqrt{1+(\hat{a}+\hat{y}_0)^2}$ are the normalized undeformed lengths of the top and bottom springs in the schematic of Fig. 1(a), respectively. The conditions given by Eqs. (7a,b) are then substituted back into Eq. (6), resulting in the following expression

$$\hat{f}_{\mathrm{DQZS}} = \hat{y}_0 \left(1 + \frac{(\hat{y}_{\mathrm{r}}-\hat{a})\left(1-\frac{\hat{l}_{01}}{\sqrt{1+(\hat{a}-\hat{y}_{\mathrm{r}})^2}}\right)}{\hat{a}\left(1-\frac{\hat{l}_{01}}{\hat{l}_{02}}\right)} + \frac{(\hat{y}_{\mathrm{r}}+\hat{a})\left(1-\frac{\hat{l}_{02}}{\sqrt{1+(\hat{a}+\hat{y}_{\mathrm{r}})^2}}\right)}{\hat{a}\left(\frac{\hat{l}_{02}}{\hat{l}_{01}}-1\right)} \right) \tag{8}$$

which only depends on the normalized size $\hat{a}$ and the normalized unloaded displacement $\hat{y}_0$.

Secondly, to achieve a DQZS behaviour, Eq. (8) is differentiated once and twice with respect to the normalized displacement $\hat{y}_{\mathrm{r}}$, and set to zero yielding

$$\frac{\partial \hat{f}_{\mathrm{DQZS}}}{\partial \hat{y}_r} = (1+(\hat{a}-\hat{y}_r)^2)^{\frac{3}{2}}\left(\hat{l}_{01}-\hat{l}_{02}\right) + (1+(\hat{a}+\hat{y}_r)^2)^{\frac{3}{2}}\left(\hat{l}_{01}-\hat{l}_{02}\right)$$

$$+\left(\hat{a}^4 - 2\hat{a}^2\left(-1+{\hat{y}_r}^2\right)+\left(1+{\hat{y}_r}^2\right)^2\right)^{3/2}\left(\frac{\hat{l}_{02}}{\hat{l}_{01}}-\frac{\hat{l}_{01}}{\hat{l}_{02}}\right)=0 \qquad (9a)$$

$$\frac{\partial^2 \hat{f}_{\mathrm{DQZS}}}{\partial {\hat{y}_r}^2} = (\hat{a}+\hat{y}_r)(1+(\hat{a}-\hat{y}_r)^2)^{\frac{5}{2}} - (\hat{a}-\hat{y}_r)(1+(\hat{a}+\hat{y}_r)^2)^{\frac{5}{2}} = 0 \qquad (9b)$$

An analytical solution to the system of Eqs. (9a,b) was not possible, thus a graphical solution is obtained by plotting the curve corresponding to Eq. (9a) in the $\hat{y}_{\mathrm{r}} - \hat{a}$ plane for different values of $\hat{y}_0$ (thin black lines) and finding the intersections with the curve corresponding to Eq. (9b) (thick red lines), as illustrated in the graph of Fig. 2.

From the graph of Fig. 2, it can be seen that, apart from a trivial solution when $\hat{y}_{\mathrm{r}} = 0$, a DQZS behaviour is achieved for values of $\hat{a}$ greater than about 0.5, which corresponds to the intersection of the thick red lines with the thin dash-dotted line, and this line corresponds to a value of $\hat{y}_0$=1.

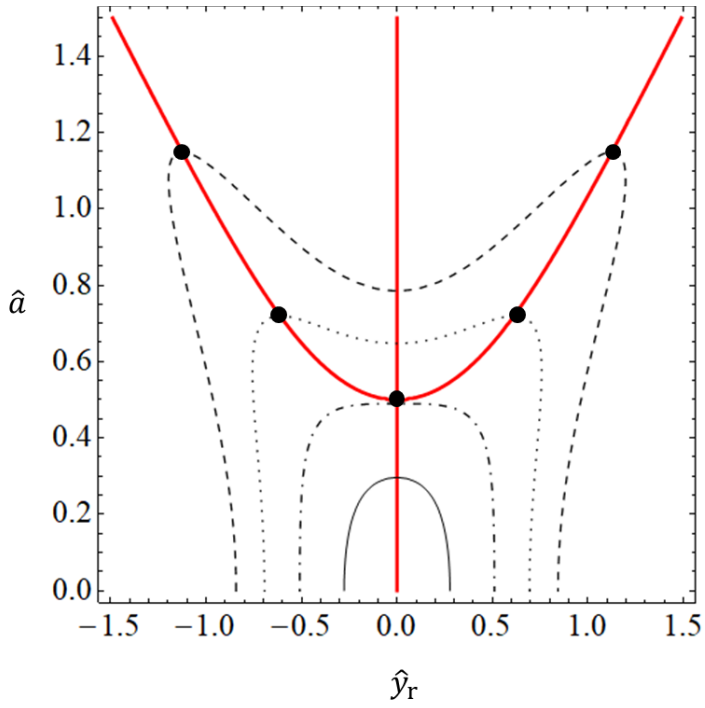

Fig. 2 Graphical solution for $\hat{y}_r$ and $\hat{a}$ to achieve a DQZS behaviour. Red thick solid lines represent Eq. (9b), thin black lines represent Eq. (9a) for $\hat{y}_0 = 0.5$ (solid line), $\hat{y}_0 = 1.0$ (dash-dotted line),

$\hat{y}_0 = 1.5$ (dotted line) and $\hat{y}_0 = 2.0$ (dashed line). Black dots indicate intersections and condition for a DQZS behaviour.

A unique configuration for the suspension system may be achieved by imposing a desired value for the stiffness $\hat{k}_1$ at $\hat{y}_\mathrm{r} = 0$. This stiffness represents the initial slope at $\hat{y}_\mathrm{r} = 0$ of the force-deflection curve, and is obtained by determining the expression for the first-order Taylor series coefficient of Eq. (8), which is given below

$$\hat{k}_1 = \frac{\hat{y}_0\left(1+\frac{\hat{a}^2\hat{l}_{01}}{(1+\hat{a}^2)^{\frac{3}{2}}}-\frac{\hat{l}_{01}}{(1+\hat{a}^2)^{\frac{1}{2}}}\right)}{\hat{a}\left(1-\frac{\hat{l}_{01}}{\hat{l}_{02}}\right)} + \frac{\hat{y}_0\left(1+\frac{\hat{a}^2\hat{l}_{02}}{(1+\hat{a}^2)^{\frac{3}{2}}}-\frac{\hat{l}_{02}}{(1+\hat{a}^2)^{\frac{1}{2}}}\right)}{\hat{a}\left(-1+\frac{\hat{l}_{02}}{\hat{l}_{01}}\right)} \tag{9c}$$

The system of Eqs. 9(a-c) is then solved numerically for different values of $\hat{k}_1$, and the solution is illustrated in the plot of Fig. 3(a) in terms of the parameters $\hat{a}, \hat{y}_0$, and $\hat{y}_{\mathrm{r,DQZS}}$, where this latter is the displacement at which the DQZS is achieved. From the plot of Fig. 3(a), it can be seen that all the length parameters increase with the increase of $\hat{k}_1$. Furthermore, the values of $\hat{y}_{\mathrm{r,DQZS}}$ are slightly lower than the values of $\hat{a}$, and this means that the DQZS region is achieved when the displacement is about the normalized length $\hat{a}$. Also, $\hat{y}_0$ is about twice the value of $\hat{a}$. The plot of Fig. 3(b) shows the resulting normalized spring stiffnesses for the two isolators. It can be seen that the lateral springs for the SQZS isolator are relatively softer than those of the DQZS isolator. This is because the springs of the DQZS isolator suspension are used to support the weight of the isolated mass as well, while for the SQZS isolator, the vertical linear spring is used for that purpose.

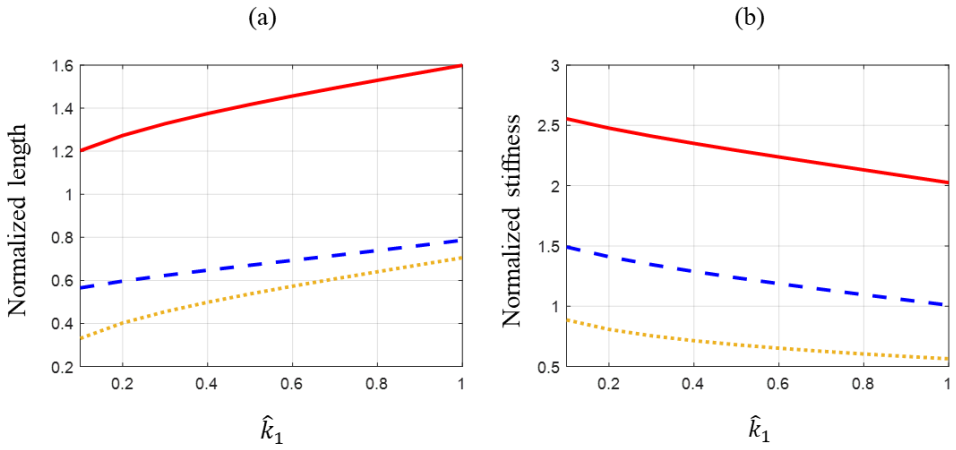

Fig. 3 (a) Normalized length parameters $\hat{y}_0$ (solid line), $\hat{a}$ (dashed line) and $\hat{y}_{\mathrm{r,DQZS}}$ (dotted line) as a function of $\hat{k}_1$ to achieve a DQZS behaviour. (b) Normalized stiffness parameters $\hat{k}_{\mathrm{s1}}$ (solid line), $\hat{k}_{\mathrm{s2}}$ (dashed line) and $\hat{k}_{\mathrm{s3}}$ (dotted line) as a function of $\hat{k}_1$.

The normalized force-deflection curve of the proposed DQSZ isolator is illustrated in the plot of Fig. 4 for three different values of $\hat{k}_1$. The plot of Fig. 4 is obtained by solving Eq. (8) and using the expressions in Eqs. (9a-c) to retrieve the dependent parameters $\hat{y}_0$ and $\hat{a}$. It can be seen that the curves in the plot of Fig. 4 resemble a sigmoidal shape. They exhibit a nonlinear behaviour with a softening characteristic, where the DQZS effect is achieved at relatively large displacements (i.e. $|\hat{y}_r|$about 0.5), as indicated by the markers. Such relatively large displacements should be compared to the relatively low ones of the SQZS counterpart, as discussed further below.

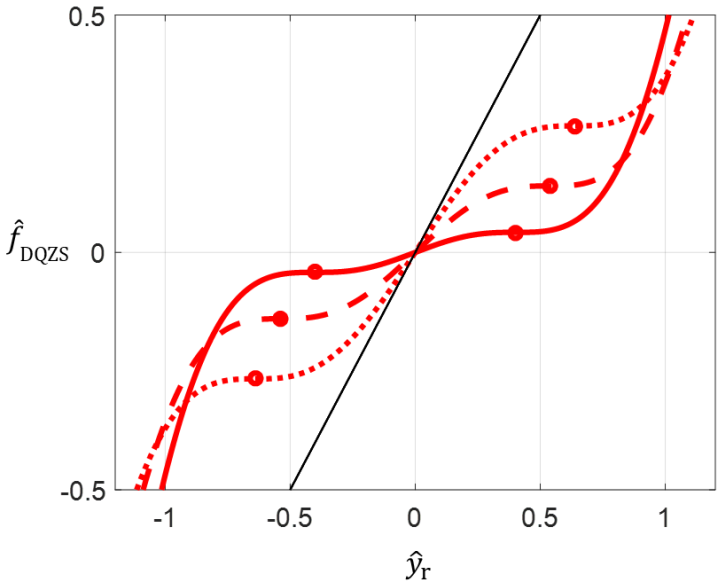

Fig. 4 Normalized force-displacement curve with DQZS behaviour, for different values of the initial stiffness: $\hat{k}_1 = 0.2$ (solid line), $\hat{k}_1 = 0.5$ (dashed line) and $\hat{k}_1 = 0.8$ (dotted line). The thin solid line represents the linear case, i.e. $\hat{k}_1 = 1$. The large dots indicate the DQZS points.

The schematics in Figs. 5(a) and (c) show two different configurations of the suspension of the proposed DQZS isolator, corresponding to the two extreme values of $\hat{k}_1$ reported in the plot of Fig. 4. Such extreme values are selected to be reasonably close to the initial stiffness of the SQZS isolator, and reasonably close to the stiffness of the linear isolator. The schematics in Figs. 5(b) and (d) show the two configurations of the suspension of the classical SQZS isolator, corresponding to the case in the schematics of Figs. 5(a) and (c), respectively. Thus the schematic of Fig. 5(a) compares to that in Fig. 5(b), and the schematic of Fig. 5(c) compares to that in Fig. 5(d). It can be seen that, for equal static displacement, the specific X-shape configuration of the four-springs in the proposed DQZS isolator, potentially allows relatively smaller spring elongation respect to the T-shape configuration of the three-springs in the classical SQZS isolator.

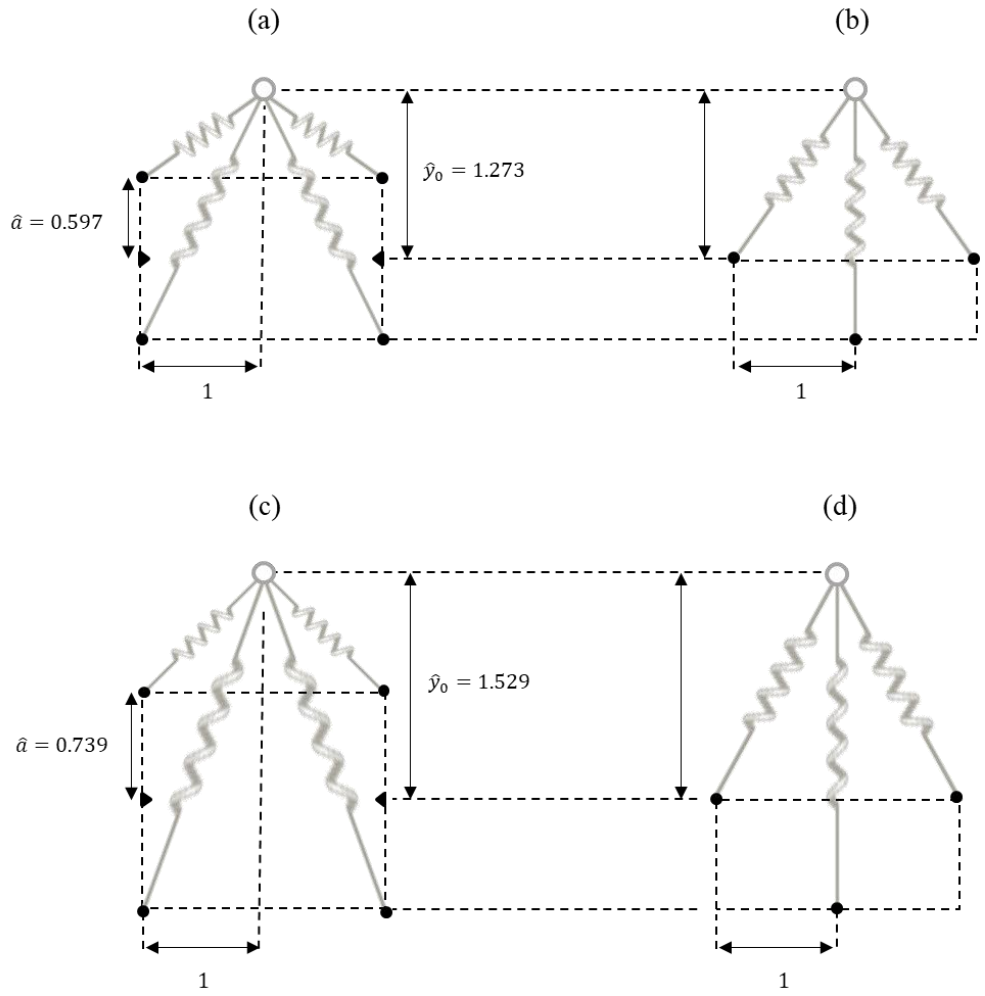

Fig. 5 Configurations of the unloaded isolator suspension with DQZS behaviour for (a) $\hat{k}_1 = 0.2$ and (b) $\hat{k}_1 = 0.8$. Configurations of the unloaded isolator suspension with SQZS behaviour for (c) $\hat{k}_1 = 0.2$ and (d) $\hat{k}_1 = 0.8$.

The comparison between the force-deflection curves of the isolators in the schematics of Figs. 5(a,b) and in Figs. 5(c,d) are reported in the plot of Fig. 6(a,b), respectively. It can be seen that the static characteristic of the proposed isolator (thick solid line) exhibits a DQZS behaviour at $|\hat{y}_r|$about 0.5, while the static characteristic of the classical isolator (thin solid line) manifest SQZS behaviour at $\hat{y}_r = 0$. The dashed lines in the plot of Fig. 6 are approximated solutions and will be discussed in the following section.

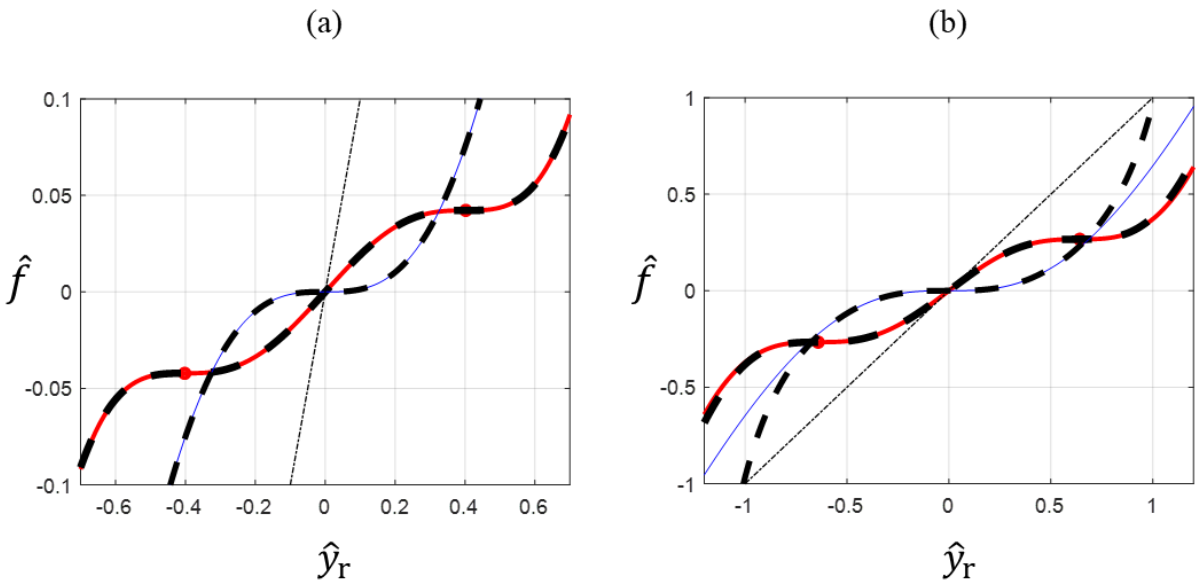

Fig. 6 Normalized force-displacement curve for (a) $\hat{k}_1 = 0.2$ and (b) $\hat{k}_1 = 0.8$ for the proposed isolator with DQZS behaviour (thick solid line) and the classical isolator with SQZS behaviour (thin solid line). The dashed lines denote polynomial approximations to the corresponding analytical solution, and the thin dash-dotted line denotes the linear case, $\hat{f} = \hat{y}_r$.

4 ISOLATOR PERFORMANCE

4.1 Approximation of the force-displacement relation

In order to investigate the dynamic response of the proposed isolator, the static force-deflection curve of Eq. (8), with the constraints given in Eqs. (9a-c), is approximated by a polynomial expression. The following boundary conditions are adopted: (i) the stiffness at $\hat{y}_r = 0$ is set equal to $\hat{k}_1$; (ii) the stiffness and its derivative at $\hat{y}_r = \hat{y}_{r,DQZS}$ are both set to zero; (iii) the force at $\hat{y}_r = \hat{y}_{r,DQZS}$ is set equal to the value obtained by Eq. (8) at $\hat{y}_r = \hat{y}_{r,DQZS}$. The following approximated seventh order (odd) polynomial expression is obtained

$$\hat{f}_{DQZS} \approx \beta_{DQZS}\hat{y}_r + \gamma_{DQZS}\hat{y}_r{}^3 + \delta_{DQZS}\hat{y}_r{}^5 + \varepsilon_{DQZS}\hat{y}_r{}^7 \tag{10}$$

where

$$\beta_{\mathrm{DQZS}} = \hat{k}_1 \tag{11a}$$

$$\gamma_{\mathrm{DQZS}} = \frac{35\hat{f}_{\mathrm{DQZS}} - 24\hat{k}_1\hat{y}_{\mathrm{r,DQZS}}}{8\hat{y}_{\mathrm{r,DQZS}}^3} \tag{11b}$$

$$\delta_{\mathrm{DQZS}} = \frac{-21\hat{f}_{\mathrm{DQZS}} + 12\hat{k}_1\hat{y}_{\mathrm{r,DQZS}}}{4\hat{y}_{\mathrm{r,DQZS}}^5} \tag{11c}$$

$$\varepsilon_{\mathrm{DQZS}} = \frac{15\hat{f}_{\mathrm{DQZS}} - 8\hat{k}_1\hat{y}_{\mathrm{r,DQZS}}}{8\hat{y}_{\mathrm{r,DQZS}}^7} \tag{11d}$$

For the classical SQZS isolator, Eq. (4) is approximated using a classical Taylor series expansion up to the seventh order, yielding

$$\hat{f}_{\mathrm{SQZS}} \approx \beta_{\mathrm{SQZS}}\hat{y}_{\mathrm{r}} + \gamma_{\mathrm{SQZS}}\hat{y}_{\mathrm{r}}{}^3 + \delta_{\mathrm{SQZS}}\hat{y}_{\mathrm{r}}{}^5 + \varepsilon_{\mathrm{SQZS}}\hat{y}_{\mathrm{r}}{}^7 \tag{12}$$

where

$$\beta_{\mathrm{SQZS}} = 0 \tag{13a}$$

$$\gamma_{\mathrm{SQZS}} = \frac{1}{2}\frac{\sqrt{1+\hat{y}_0{}^2}}{\sqrt{1+\hat{y}_0{}^2}-1} \tag{13b}$$

$$\delta_{\mathrm{SQZS}} = -\frac{3}{8}\frac{\sqrt{1+\hat{y}_0{}^2}}{\sqrt{1+\hat{y}_0{}^2}-1} \tag{13c}$$

$$\varepsilon_{\mathrm{SQZS}} = \frac{5}{16}\frac{\sqrt{1+\hat{y}_0{}^2}}{\sqrt{1+\hat{y}_0{}^2}-1} \tag{13d}$$

The approximated polynomial in Eq. (10) for the DQZS isolator is also plotted in Fig. 6(a) and (b) as thick dashed lines and compared to the exact analytical expression drawn as thick solid lines. In the plots of Fig. 6(a) and (b), the approximated force deflection curves of the classical SQZS isolator from Eq. (12) are also plotted as thick dashed lines and compared to the exact expression from Eq. (4) as thin solid lines. It can be noted that both polynomial expressions approximate relatively well the corresponding exact curves. However, when the displacement achieves relatively large values, the Taylor series approximation in Eq. (12), for the classical SQZS T-shape isolator,

starts deviating from the exact behaviour, as visible in the plot of Fig. 6(b), although this is a working region where the classical SQZS isolator is usually not designed for.

4.2 Equation of motion

The equation of motion of the systems depicted in the schematics of Fig. 1(a) and (b) is given by

$$m\ddot{y}_\mathrm{r} + c\dot{y}_\mathrm{r} + f = -m\ddot{y}_\mathrm{e}, \tag{14}$$

where f is the static spring restoring force given by either Eq. (1) or (5), the overdots denote first and second derivative respect to time *t*, and a viscous damping coefficient *c* is introduced to account for energy dissipation. Both isolators are assumed to be excited at the base by a harmonic displacement $y_\mathrm{e} = Y_\mathrm{e}\cos(\omega t + \varphi)$, as depicted in the schematic of Fig. 1, where Y_e is the amplitude, ω is the angular frequency, and φ is the phase.

By using the approximate expression for the spring restoring force, given in Eq. (10) for the DQZS isolator and in Eq. (12) for the SQZS isolator, Eq. (14) is written in the following normalized form

$$\hat{y}_\mathrm{r}'' + 2\zeta\hat{y}_\mathrm{r}' + \beta\hat{y}_\mathrm{r} + \gamma\hat{y}_\mathrm{r}^3 + \delta\hat{y}_\mathrm{r}^5 + \varepsilon\hat{y}_\mathrm{r}^7 = \hat{\omega}^2\hat{Y}_\mathrm{e}\cos(\hat{\omega}\hat{t} + \varphi) \tag{15}$$

where $\hat{t} = \omega_0 t$ and $\hat{\omega} = \frac{\omega}{\omega_0}$ are the normalized time and angular frequency respectively, $\omega_0 = \sqrt{\frac{k_{s0}}{m}}$, $\zeta = \frac{c}{2m\omega_0}$ is the damping ratio, $\hat{Y}_\mathrm{e} = \frac{Y_\mathrm{e}}{d}$ is the normalized displacement amplitude of the excitation, and primes denote differentiation respect to $\hat{t}$.

In particular, for the DQZS isolator, $\beta, \gamma, \delta, \varepsilon$ are given by Eqs. (11a-d), while for the SQZS isolator they are given by Eqs. (13a-d), and for the linear system $\beta = 1$and $\gamma = \delta = \varepsilon = 0$.

4.3 Displacement transmissibility

The displacement transmissibility of the isolator is used as a metric to assess the isolator performance. The displacement transmissibility (Lu et al., 2016) is defined as the ratio of the displacement amplitude of the suspended mass to that of the moving base, i.e. the external frame. To solve Eq. (15), it is assumed that the system response is predominately harmonic at the excitation frequency, so that $\hat{y}_{\mathrm{r}} = \hat{Y}_{\mathrm{r}} \cos(\hat{\omega}\hat{t})$ (where $\hat{Y}_{\mathrm{r}}$ is the relative displacement amplitude), and this is substituted back into Eq. (15), where a first-order harmonic balance approximation is applied to yield

$$\hat{\omega}^4 \left[\hat{Y}_{\mathrm{r}}{}^2 - \hat{Y}_{\mathrm{e}}{}^2 \right] + 2\hat{Y}_{\mathrm{r}}{}^2 \hat{\omega}^2 [2\zeta^2 - G] + G^2 \hat{Y}_{\mathrm{r}}{}^2 = 0 \tag{16}$$

with $G = \beta + \frac{3}{4}\gamma \hat{Y}_{\mathrm{r}}{}^2 + \frac{5}{8}\delta \hat{Y}_{\mathrm{r}}{}^4 + \frac{35}{64}\varepsilon \hat{Y}_{\mathrm{r}}{}^6$.

Equation (16) is quadratic in $\hat{\omega}^2$and can be solved in closed form to give the relation between the relative displacement transmissibility $\frac{\hat{Y}_{\mathrm{r}}}{\hat{Y}_{\mathrm{e}}}$ and the frequency.

By defining the normalized absolute displacement of the suspended mass as $\hat{y}_{\mathrm{a}} = \hat{y}_{\mathrm{e}} + \hat{y}_{\mathrm{r}} = \hat{Y}_{\mathrm{a}} \cos(\hat{\omega}\hat{t} + \vartheta)$, the absolute displacement transmissibility is determined as

$$\frac{\hat{Y}_{\mathrm{a}}}{\hat{Y}_{\mathrm{e}}} = \sqrt{1 - \frac{\hat{Y}_{\mathrm{r}}{}^2}{\hat{Y}_{\mathrm{e}}{}^2} + \frac{2G}{\hat{\omega}^2} \frac{\hat{Y}_{\mathrm{r}}{}^2}{\hat{Y}_{\mathrm{e}}{}^2}} \tag{17}$$

The isolation performance is then compared in terms of the absolute displacement transmissibility for the DQZS isolator, the SQZS isolator, and the linear system, as functions of the normalized frequency $\hat{\omega}$. The absolute displacement transmissibility is calculated and shown in the plots of Fig. 7(a) and 7(b) for $\hat{k}_1 = 0.2$, $\hat{Y}_e = 0.5$ and for two different values of damping.

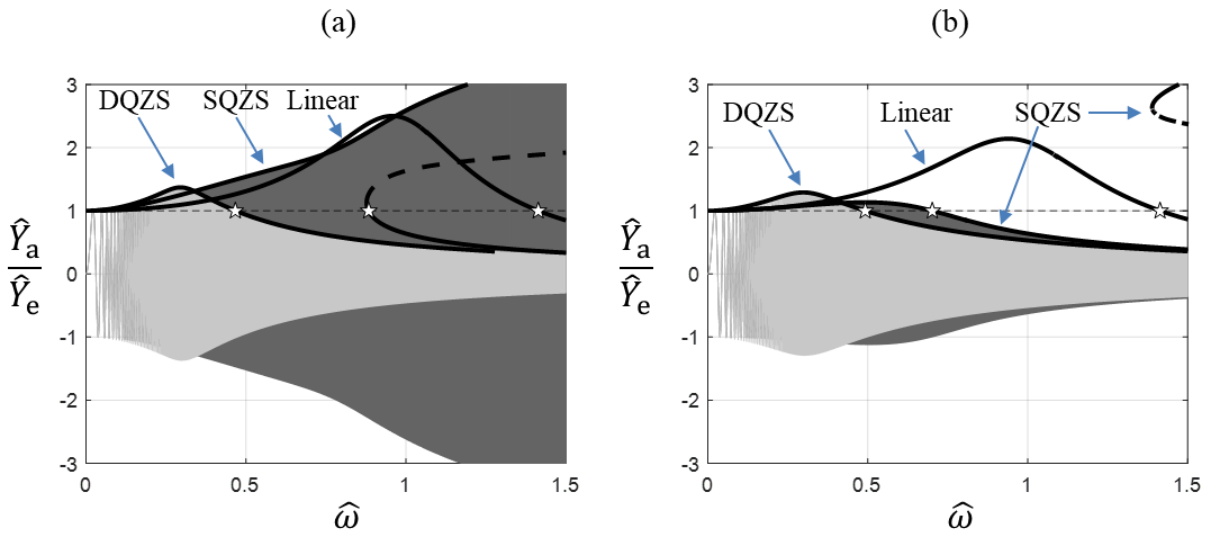

Fig. 7 Absolute displacement transmissibility of the DQZS isolator compared to that of the SQZS isolator, and to that of the linear system, for $\hat{k}_1 = 0.2$, $\hat{Y}_e = 0.5$ and: (a) $\zeta = 0.9\,\zeta^*$ and (b) $\zeta = 1.1\,\zeta^*$. Numerical solutions to a slow sine sweep excitation (thin lines). Isolation region is for frequencies $\hat{\omega} > \hat{\omega}^*$, which is denoted by a star.

The damping values in the plots of Fig. 7(a) and 7(b) are respectively selected to be 0.9 and 1.1 times the critical value for an unbounded response of the SQZS isolator, which is given in (Milovanovic et al., 2009) by the following approximate expression $\zeta^* = \hat{Y}_e\sqrt{\frac{3}{16}}\sqrt{\frac{\sqrt{1+\hat{y}_0{}^2}}{2\left(\sqrt{1+\hat{y}_0{}^2}-1\right)}}$.

Although this is valid for a SQZS isolator with cubic stiffness nonlinearity only (while in this paper a 7-th order approximation is adopted), it gives a rough estimate for such a threshold. On the one hand, in the plot of Fig. 7(a), it can be thus clearly seen that if the damping is lower than the critical value ζ^*, the response of the SQZS isolator increases indefinitely with the increase of frequency. In this case the system is still stable, but its response in not limited in amplitude, i.e. it is unbounded. On the other hand, in the plot of Fig. 7(b), it can be seen that if the damping is larger than ζ^*, then the response of the SQZS isolator is bounded, and a fair comparison can be done with the response of the DSQZ isolator. However, from the plot in Fig. 7(b) it can also be noted that at about $\hat{\omega} = 1.5$

a detached curve appears for the classical SQZS isolator at higher amplitudes, which is highly undesirable. In the range of parameters shown, no detached resonance curve was identified for the proposed DQZS isolator. For validation purposes, numerical simulations are performed by applying a slow sine sweep excitation to the equation of motion, and the resulting transmissibility is also plotted in Fig. 7 as thin lines.

An increase of damping in a vibration isolator would be generally detrimental for the performance above the isolation frequency, and thus a value of $\zeta = 1.1\,\zeta^*$ is selected for the following analysis.

To investigate the effect of the non-dimensional stiffness $\hat{k}_1$ on the isolation performance, the absolute displacement transmissibility is shown in the plots of Fig. 8(a) and 8(b) for $\hat{Y}_e = 0.6$, and for $\hat{k}_1 = 0.2$ and $\hat{k}_1 = 0.6$, respectively. It can be seen that a lower value of $\hat{k}_1$ is generally desirable, as this is related to the initial stiffness in the force-displacement curve and thus to the linearized resonance frequency, which increases as $\hat{k}_1$ increases.

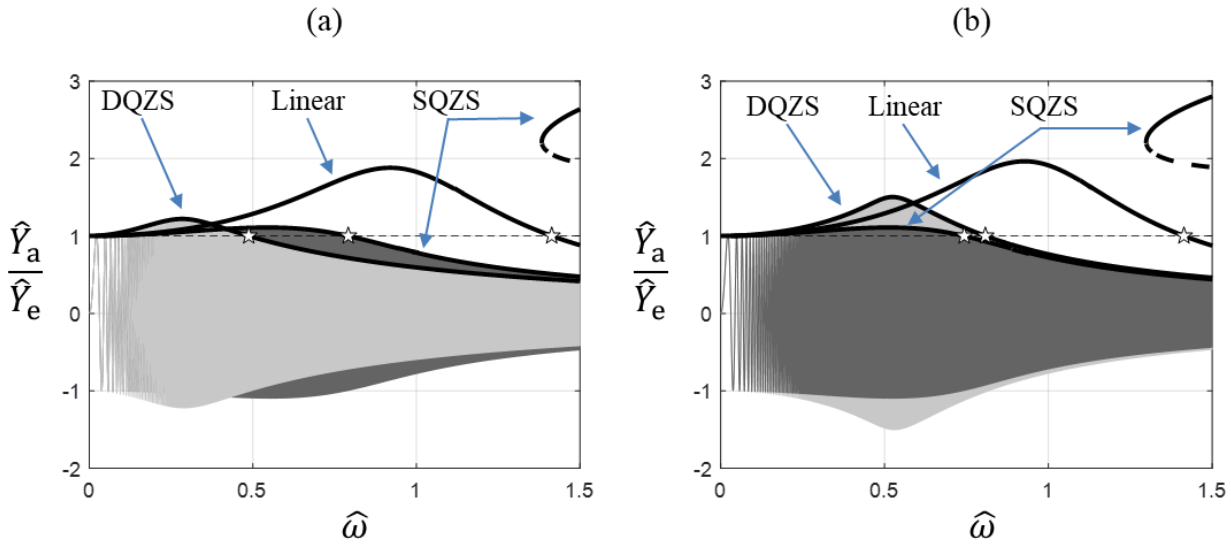

Fig. 8 Absolute displacement transmissibility of the DQZS isolator compared to that of the SQZS isolator, and to that of the linear system, for $\hat{Y}_e = 0.6$ and: (a) $\hat{k}_1 = 0.2$ and (b) $\hat{k}_1 = 0.6$. Numerical solutions to a slow sine sweep excitation (thin lines). Isolation region is for frequencies $\hat{\omega} > \hat{\omega}^*$, which is denoted by a star.

To investigate the effect of the non-dimensional amplitude of excitation $\widehat{Y}_e$ on the isolation performance, the absolute displacement transmissibility is shown in the plots of Fig. 9(a) and 9(b) for $\hat{k}_1 = 0.2$, and for $\widehat{Y}_e = 0.6$ and $\widehat{Y}_e = 0.2$, respectively.

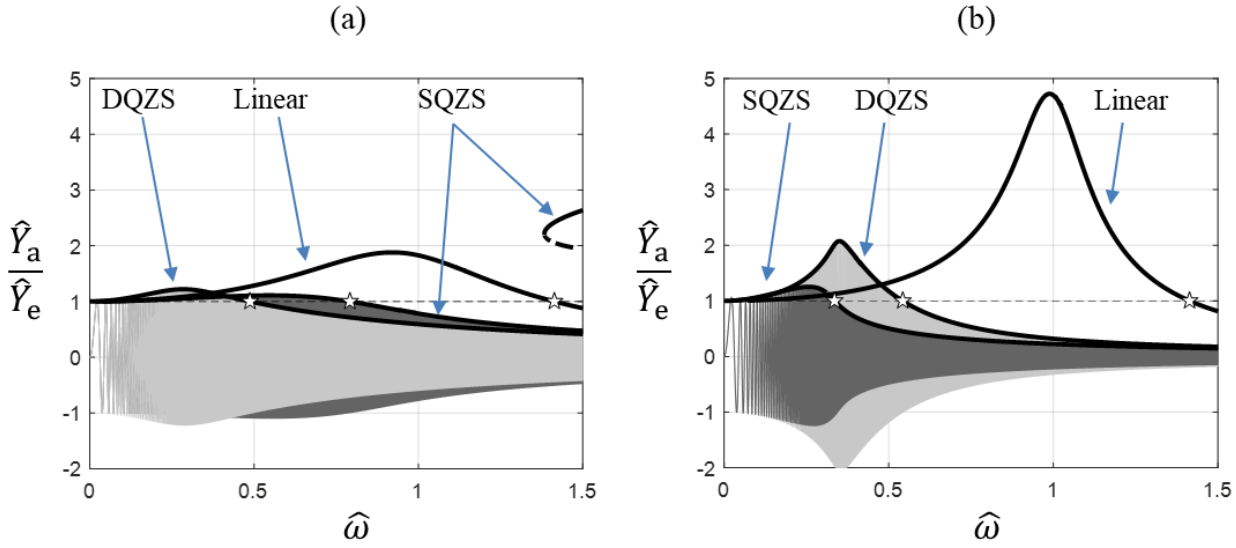

Fig. 9 Absolute displacement transmissibility of the DQZS isolator compared to that of the SQZS isolator, and to that of the linear system, for $\hat{k}_1 = 0.2$ and: (a) $\widehat{Y}_e = 0.6$ and (b) $\widehat{Y}_e = 0.2$. Numerical solutions to a slow sine sweep excitation (thin lines). Isolation region is for frequencies $\hat{\omega} > \hat{\omega}^*$, which is denoted by a star.

It can be seen that the proposed DQZS isolator outperforms the classical SQZS isolator, in terms of a larger isolation region, for relatively higher values of excitation amplitudes. In particular, the excitation amplitude in the plot of Fig. 9(a) is three times that in the plot of Fig. 9(b). Nonetheless, the isolation region (i.e. the frequency region where $\frac{\hat{Y}_a}{\hat{Y}_e} < 1$) of the proposed DQZS isolator is larger than that of the classical SQZS isolator in the plot of Fig. 9(a), while it is smaller in that of Fig. 9(b).

Such an advantage is achieved due to the particular shape of the force-deflection curve of the DQZS isolator, which may be designed to extend the overall region of low stiffness. In particular, when the

amplitude of vibration is relatively small, then the classical SQZS isolator outperforms the proposed DQZS isolator, since the stiffness around the equilibrium configuration for the classical SQZS isolator is very small, while that of the proposed DQZS isolator is relatively large. However, when the amplitude of vibration is relatively large, then the stiffness of the classical SQZS isolator rapidly increases in a hardening way, while that of the proposed DQZS isolator decreases in a softening way. As a consequence, for high vibration amplitudes, the proposed DQZS isolator outperforms the corresponding classical SQZS isolator.

4.4 Isolation region

To better quantify and compare the isolation regions for the different isolators, the isolation frequency $\widehat{\omega}^*$ is introduced and defined as the frequency where the displacement transmissibility is equal to 1. To visualize the location if this frequency on the transmissibility curves, it was plotted in Fig. 7, Fig. 8 and Fig. 9 as a star, and a horizontal thin dashed line was also plotted for reference, indicating the transmissibility equal to 1.

For a linear isolator this frequency is well known, and it is given by $\sqrt{2} \approx 1.41$. For the nonlinear systems, it is determined by setting to 1 the absolute displacement transmissibility in Eq. (17) yielding

$$\widehat{\omega}^* = \sqrt{2G} \tag{18a}$$

Equation (18a) is then substituted back into Eq. (16) to give

$$8\hat{Y}_{\mathrm{r}}{}^2\zeta^2 + \hat{Y}_r{}^2 G - 4G\hat{Y}_e{}^2 = 0 \tag{18b}$$

which can be solved numerically for $\hat{Y}_{\mathrm{r}}{}^2$.

The frequency $\hat{\omega}^*$ is thus plotted in Fig. 10(a) and 10(b) as a function of the stiffness $\hat{k}_1$, for two different values of excitation amplitudes. The lower the frequency $\hat{\omega}^*$ the larger the region where isolation is achieved. In the plot of Fig. 10(a), it can be seen how the isolation region of the SQZS isolator is always larger than that of the DQZS isolator for $\hat{Y}_e = 0.2$. However, when the excitation amplitude increases to $\hat{Y}_e = 0.5$ as in the plot of Fig. 10(b), the isolation region of the DQZS isolator is larger than that of the SQZS isolator for $\hat{k}_1$ smaller than about 0.4.

A performance index $\Delta\hat{\omega}^*$ is defined below as the relative difference between the frequency $\hat{\omega}^*$ of the DQZS isolator and that of the SQZS isolator. This gives

$$\Delta\hat{\omega}^* = \frac{\hat{\omega}^*_{\mathrm{DQZS}} - \hat{\omega}^*_{\mathrm{SQZS}}}{\hat{\omega}^*_{\mathrm{SQZS}}} \tag{19}$$

where the sub-script denotes the specific isolator. Equation (19) is plotted in Fig. 11 as a function of $\hat{k}_1$ for increasing values of the excitation amplitude. Negative values of $\Delta\hat{\omega}^*$ (white region) mean smaller values of $\hat{\omega}^*$ for the DQZS isolator relative to the SQZS isolator, and thus larger isolation region for the DQZS isolator relative to the SQZS isolator. It can be seen that, generally, a better performance of the DQZS isolator is achieved for high values of the excitation amplitude, $\hat{Y}_e$, and lower values of stiffness, $\hat{k}_1$. In the plots of Figs. 7, 8, 9 and 10, the lower the value of $\hat{\omega}^*$, the larger the isolation region and the better the performance of the isolator. In the plot of Fig. 11, negative values for $\Delta\hat{\omega}^*$ mean better isolation region for the DQZS isolator respect to the SQZS isolator.

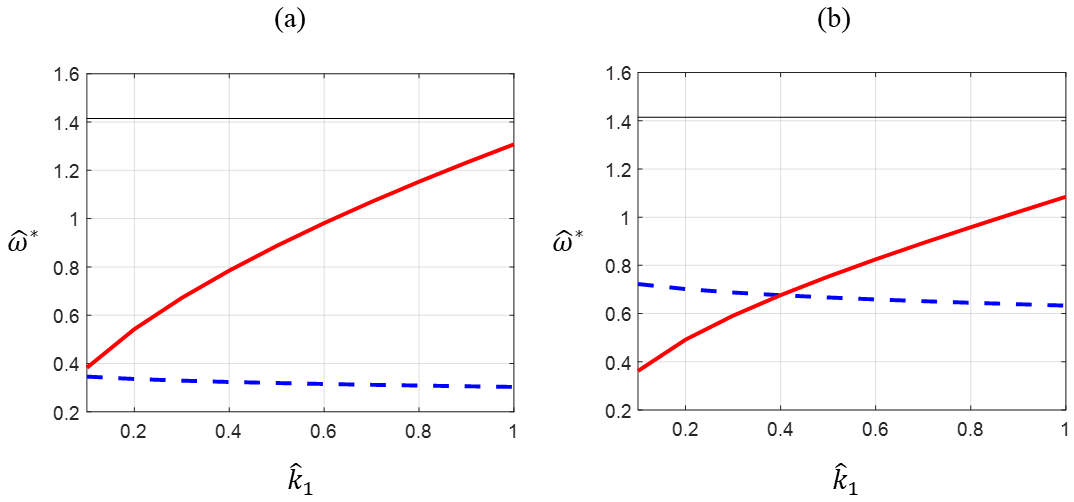

Fig. 10 Normalized frequency $\widehat{\omega}^*$, denoting isolation region, as a function of $\hat{k}_1$ for (a) $\hat{Y}_e = 0.2$ and (b) $\hat{Y}_e = 0.5$. DQZS isolator (thick solid line), SQZS isolator (thick dashed line) and linear isolator (thin solid line).

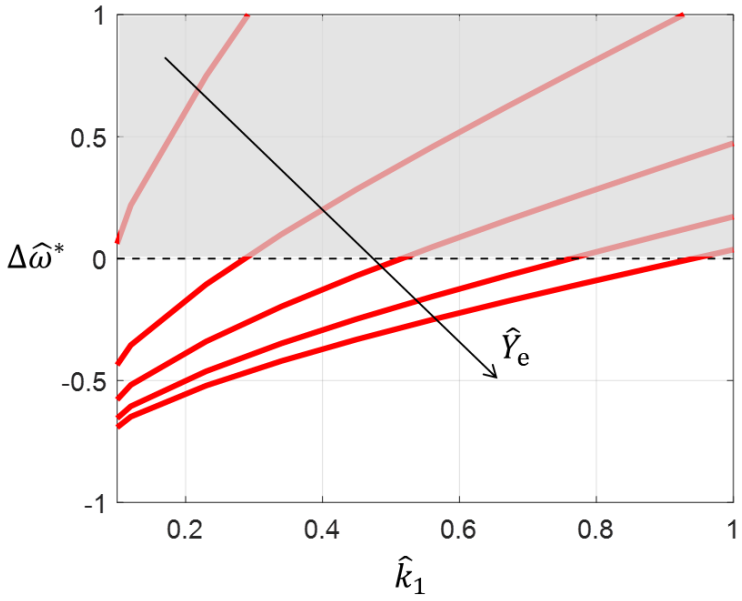

Fig. 11 Index $\Delta\widehat{\omega}^*$ to quantify isolation performance of the DQZS isolator relative to the SQZS isolator, as a function of $\hat{k}_1$ for increasing values of excitation amplitude, as denoted by the arrow: $\hat{Y}_e = 0.2, 0.4, 0.6, 0.8, 0.9$. The white region indicates superior performance of the proposed DQZS isolator respect to the classical SQZS one.

5 CONCLUSIONS

This paper has investigated the static and dynamic characteristics of the nonlinear suspension of a vibration isolator consisting of four linear springs arranged in a X-shaped configuration to achieve a sigmoidal shape force-deflection characteristic with DQZS behaviour at large deflections.

The analytical insight has allowed to highlight the fundamental key-parameters affecting the performance of the isolator. The dynamic analysis is performed analytically in terms of the frequency response of the system, and of its displacement transmissibility.

The performance of the proposed DQZS isolator is compared to that of the classical SQZS isolator, with low stiffness at the equilibrium configuration. It has been shown that, in case of relatively large amplitudes of vibration, the sigmoidal shape characteristic of the proposed DQZS elastic suspension is responsible of enlarging the isolation region, compared to that of the classical SQZS isolator, thus providing better isolation performance. For the range of parameters used, a reduction of about 50% can be achieved in terms of isolation frequency. Alternatively, for a given excitation amplitude, the adoption of the proposed DQZS suspension leads to a more compact design. This is due to the softening effect of the force-deflection curve. Numerical results have confirmed the validity of the approximate analytical formulation, providing a useful insight for the design of such DQZS isolator.

Declaration of conflicting interests: the authors declare that there is no conflict of interest.

Funding: this research received no specific grant from any funding agency in the public, commercial, or not-for-profit sectors.

REFERENCES

Dai H, Jing X, Wang Y et al. (2018) Post-capture vibration suppression of spacecraft via a bio-inspired isolation system. *Mechanical Systems and Signal Processing* 105: 214–240. DOI: 10.1016/j.ymssp.2017.12.015

Gatti G (2019) A K-shaped spring configuration to boost elastic potential energy. *Smart Materials and Structures* 28: 077002. DOI: 10.1088/1361-665X/ab1ec8

Gatti G (2020) Statics and dynamics of a nonlinear oscillator with quasi-zero stiffness behaviour for large deflections. C*ommunications in nonlinear science and numerical simulation* 83: 105143. DOI: 10.1016/j.cnsns.2019.105143

Gatti G (2021a) Optimizing elastic potential energy via geometric nonlinear stiffness, *Communications in Nonlinear Science and Numerical Simulation* 103: 106035. DOI: 10.1016/j.cnsns.2021.106035

Gatti G (2021b) Effect of Parameters on the Design of a Suspension System with Four Oblique Springs. *Shock and Vibration* 2021: 5556088. DOI: 10.1155/2021/5556088

Gatti G, Shaw AD, Gonçalves PJP et al. (2022) On the detailed design of a quasi-zero stiffness device to assist in the realisation of a translational Lanchester damper. *Mechanical Systems and Signal Processing* 164: 108258. DOI: 10.1016/j.ymssp.2021.108258

Gatti G (2022) An adjustable device to adaptively realise diverse nonlinear force-displacement characteristics. *Mechanical Systems and Signal Processing* 180: 109379. DOI: 10.1016/j.ymssp.2022.109379

Ibrahim RA (2008) Recent advances in nonlinear passive vibration isolators. *Journal of Sound and Vibration* 314: 371–452. DOI: 10.1016/j.jsv.2008.01.014

Jing X, Chai Y, Chao X et al. (2022) In-situ adjustable nonlinear passive stiffness using X-shaped mechanisms. *Mechanical Systems and Signal Processing* 170: 108267. DOI: 10.1016/j.ymssp.2021.108267

Kovacic I, Brennan MJ and Waters TP (2008) A study of a nonlinear vibration isolator with a quasi-zero stiffness characteristic. *Journal of Sound and Vibration* 315: 700–711. DOI: 10.1016/j.jsv.2007.12.019

Li M, Cheng W and Xie R (2020) Design and experiments of a quasi–zero stiffness isolator with a noncircular cam based negative-stiffness mechanism. *Journal of Vibration and Control* 26(21–22): 1935–1947. DOI: 10.1177/1077546320908689

Liu X, Huang X and Hua H (2013) On the characteristics of a quasi-zero stiffness isolator using Euler buckled beam as negative stiffness corrector. *Journal of Sound and Vibration* 332(14): 3359–3376. DOI: 10.1016/j.jsv.2012.10.037

Liu X, Huang X, and Hua H (2014) Performance of a zero stiffness isolator under shock excitations. *Journal of Vibration and Control* 20(14): 2090–2099. DOI: 10.1177/1077546312473767

Lu Z-Q, Brennan MJ and Chen L-Q (2016) On the transmissibilities of nonlinear vibration isolation system. *Journal of Sound and Vibration* 375: 28–37. DOI: 10.1016/j.jsv.2016.04.032

Lu Z-Q, Hu G-S, Ding H et al. (2019) Jump-based estimation for nonlinear stiffness and damping parameters. *Journal of Vibration and Control* 25(2): 325–335. DOI: 10.1177/1077546318777414

Milovanovic Z, Kovacic I and Brennan MJ (2009) On the displacement transmissibility of a base excited viscously damped nonlinear vibration isolator. *Journal of Vibration and Acoustics* 131(5): 054502. DOI: 10.1115/1.3147140

Mofidian SMM and Bardaweel H (2018) Displacement transmissibility evaluation of vibration isolation system employing nonlinear-damping and nonlinear-stiffness elements. *Journal of Vibration and Control* 24(18): 4247–4259. DOI: 10.1177/1077546317722702

Shaw AD, Gatti G, Gonçalves PJP et al. (2021) Design and test of an adjustable quasi-zero stiffness device and its use to suspend masses on a multi-modal structure. *Mechanical Systems and Signal Processing* 152: 107354. DOI: 10.1016/j.ymssp.2020.107354

Shi X, Xu J, Chen T et al. (2022) Novel low frequency bionic vibration isolation structure. *Journal of Vibration and Control*. Epub ahead of print 7 May 2022. DOI: 10.1177/10775463221095325

Song Y, Zhang C, Li Z et al. (2022) Study on dynamic characteristics of bio-inspired vibration isolation platform. *Journal of Vibration and Control* 28(11–12): 1470–1485. DOI: 10.1177/1077546321993614

Tang B and Brennan MJ (2013) A comparison of two nonlinear damping mechanisms in a vibration isolator. *Journal of Sound and Vibration* 332(3,4): 510-520. DOI: 10.1016/j.jsv.2012.09.010

Wang Y, Li H-X, Cheng C et al. (2021) A nonlinear stiffness and nonlinear inertial vibration isolator. *Journal of Vibration and Control* 27(11–12): 1336–1352. DOI: 10.1177/1077546320940924

Xu D, Zhang Y, Zhou J et al. (2014) On the analytical and experimental assessment of the performance of a quasi-zero-stiffness isolator. *Journal of Vibration and Control* 20(15): 2314–2325. DOI: 10.1177/1077546313484049

Yan G, Zou H-X, Wang S et al. (2020) Large stroke quasi-zero stiffness vibration isolator using three-link mechanism. *Journal of Sound and Vibration* 478: 115344. DOI: 10.1016/j.jsv.2020.115344

Yan G, Zou H-X, Wang S et al. (2021) Bio-inspired vibration isolation: Methodology and design. *Applied Mechanics Reviews* 73: 020801. DOI: 10.1115/1.4049946

Yang Z, Wang Y, Huang Z, et al. (2021) Characteristic analysis of a new high-static-low-dynamic stiffness vibration isolator based on the buckling circular plate. *Journal of Low Frequency Noise, Vibration and Active Control* 40(3): 1526–1539. DOI: 10.1177/1461348420904864

Zhang X, Cao D, Liu M et al. (2022a) Vibration isolation performance of simply supported beam installed with a negative stiffness device. *Journal of Vibration and Control*. Epub ahead of print 24 February 2022. DOI: 10.1177/10775463211069396

Zhang Z, Shi F, Yang C. et al. (2022b) Quasi-zero stiffness isolator based on bistable structures with variable cross-section. *Journal of Low Frequency Noise, Vibration and Active Control* 41(1): 405–416. DOI: 10.1177/14613484211038404

Zhao F, Ji J, Luo Q et al. (2021a) An improved quasi-zero stiffness isolator with two pairs of oblique springs to increase isolation frequency band. *Nonlinear Dynamics* 104: 349–365. DOI: 10.1007/s11071-021-06296-4

Zhao F, Ji J, Ye K et al. (2021b) An innovative quasi-zero stiffness isolator with three pairs of oblique springs. *International Journal of Mechanical Sciences* 192: 106093. DOI: 10.1016/j.ijmecsci.2020.106093

Zhao L, Yu Y, Zhou C et al. (2018) Modelling and validation of a seat suspension with rubber spring for off-road vehicles. *Journal of Vibration and Control* 24(18): 4110–4121. DOI: 10.1177/1077546317719348

Zou D, Liu G, Rao Z et al. (2021) A device capable of customizing nonlinear forces for vibration energy harvesting, vibration isolation, and nonlinear energy sink. *Mechanical Systems and Signal Processing* 147: 107101. DOI: 10.1016/j.ymssp.2020.107101

Zhu R, Marchesiello S, Anastasio D, et al. (2022) Nonlinear system identification of a double-well Duffing oscillator with position-dependent friction. *Nonlinear Dynamics* 108: 2993–3008. DOI: 10.1007/s11071-022-07346-1